World Scientific
www.worldscientific.com

ENHANCING THE YIELD OF HIGH-DENSITY ELECTRODE ARRAYS THROUGH AUTOMATED ELECTRODE SELECTION

GERT VAN DIJCK[*,§], KARSTEN SEIDL[†], OLIVER PAUL[†], PATRICK RUTHER[†],
MARC M. VAN HULLE[*] and REINOUD MAEX[‡,¶]

[*]*Computational Neuroscience Research Group*
Laboratorium voor Neuro-en Psychofysiologie
Katholieke Universiteit Leuven
Herestraat 49, 3000 Leuven, Belgium

[†]*Microsystem Materials Laboratory*
Department of Microsystems Engineering (IMTEK)
University of Freiburg
Georges-Koehler-Allee 103, 79110 Freiburg, Germany

[‡]*Science and Technology Research Institute*
University of Hertfordshire, College Lane
Hatfield AL10 9AB, United Kingdom
[§]*gert.vandijck@med.kuleuven.be*
[¶]*r.maex1@herts.ac.uk*

Recently developed CMOS-based microprobes contain hundreds of electrodes on a single shaft with inter-electrode distances as small as $30\,\mu$m. So far, neuroscientists needed to select electrodes manually from hundreds of electrodes. Here we present an electronic depth control algorithm that allows to select electrodes automatically, hereby allowing to reduce the amount of data and locating those electrodes that are close to neurons. The electrodes are selected according to a new penalized signal-to-noise ratio (PSNR) criterion that demotes electrodes from becoming selected if their signals are redundant with previously selected electrodes. It is shown that, using the PSNR, interneurons generating smaller spikes are also selected. We developed a model that aims to evaluate algorithms for electronic depth control, but also generates benchmark data for testing spike sorting and spike detection algorithms. The model comprises a realistic tufted pyramidal cell, non-tufted pyramidal cells and inhibitory interneurons. All neurons are synaptically activated by hundreds of fibers. This arrangement allows the algorithms to be tested in more realistic conditions, including backgrounds of synaptic potentials, varying spike rates with bursting and spike amplitude attenuation.

Keywords: Neural network connectivity; neural network model; spike detection; spike sorting; spike train similarity.

1. Introduction

Microelectrode arrays are able to monitor the simultaneous spiking activity of many neurons and are therefore in a position to provide valuable insights into the interaction of different brain areas.[1,2] Electrode arrays typically consist of tens of electrodes with inter-electrode distances ranging from 100 to $500\,\mu$m.[3] Recent advances in CMOS-based technology allow microprobes to be realized with up to 500 electrodes on a single shaft with inter-electrode distances (called the inter-electrode pitch) as small as $30\,\mu$m.[4–6] Such microprobes are currently used for *in vivo* recordings.[6]

After insertion of the probes active neurons need to be searched for and during the course of chronic recordings signal quality may degrade due to tissue drift or relaxation,[7] as well as inflammation or gliosis.[8] Therefore, a position adjustment of the

electrode is mandatory to obtain and maintain a good signal quality among different electrodes.

For this purpose, two different approaches are followed: (1) a mechanical adjustment of the electrode position[9–12] called 'mechanical depth control' (MDC) or (2) a selection of electrodes among a larger number of electrodes, called 'electronic depth control' (EDC), as originally proposed in Ref. 13. The EDC was developed in the framework of the Neuro-Probes project[14,15] and successfully demonstrated in Refs. 4–6.

In the case of MDC, single shafts carrying multiple microelectrodes can be repositioned independently within the neural tissue. However, all electrodes on a shaft are translated in parallel. In contrast, the EDC system concept allows electronic switching between individual microelectrodes of the same shaft, without the need to reposition either the shaft or the entire probe. As the EDC systems presented in Refs. 4–6 allow eight electrodes per shaft to be selected among hundreds of available electrodes, it is requested to find those electrodes that are closest to firing neurons. So far, this electrode selection is done manually by the neuroscientists without an automatic assistance that selects those recording sites that have the best 'quality' or that are most 'interesting' to the experimenter.

An objective validation of electronic depth control, more precisely, its capacity to select electrodes that reflect the true underlying configuration of firing neurons, has not been presented so far. In order to arrive at such a validation, we have built a biologically realistic model. The extracellular potential is the result of the integration of signals from both the soma and the dendritic tree.[2] This complex origin of spikes in the extracellular space is taken into account by using realistic models that rely upon the complexity of the cell's geometry. All cells in the presented network were excited in a realistic manner by the activation of hundreds of synapses on their dendrites, unlike those of other studies[7,26,30,31] which received excitatory current through an electrode inserted into their soma.

To summarize, the purpose of this article is (1) to build a biologically realistic model in which different neuron classes generate spikes with different shapes during synaptic stimulation, and in which both the neurons and the network have a sufficient dynamics to test the effects of fleeting variations in spike rate and synchrony and (2) to use the model to objectively validate candidate algorithms for electronic depth control. Furthermore, because the spike time stamps generated by the model are exactly known as well as the number of neurons, the developed model can serve more generally as a benchmark for spike sorting and spike detection algorithms.

2. Materials and Methods

We first review in Sec. 2.1 the architecture of the micro-electrode probes and the circuitry enabling electronic depth control. Sec. 2.2 introduces the neuronal network model used to generate biologically realistic extracellular potentials. Secs. 2.3 and 2.4 explain spike detection and spike sorting algorithms applied to the time-series generated by the model.

Section 3.1 shows that the model is capable of demonstrating spike amplitude attenuation behavior. Electrode selection using a traditional SNR criterion is presented in Sec. 3.2, the improved version is presented in Sec. 3.3.

2.1. *NeuroProbes electrode configuration for electronic depth control*

The CMOS-based probe arrays enabling electronic depth control (EDC) have a similar architecture to the passive probes developed within the Neuro-Probes project.[14,16–18] The probes comprise slender needle-like probe shafts made of silicon with a width and thickness of $180 \,\mu\text{m}$ and $100 \,\mu\text{m}$, respectively. They are available as one-dimensional (1D) and two-dimensional (2D) probe arrays, i.e. single-shaft probes and four-shaft probe combs, respectively. Two columns of 92 circular electrodes with a diameter of $20 \,\mu\text{m}$ and a pitch of $40.7 \,\mu\text{m}$, in addition to four equally-sized electrodes in the tip region, are arranged along the 4-mm-long probe resulting in a total number of 188 recording sites per probe shaft. As illustrated in Fig. 1 for a single-shaft probe, the shafts are connected to a wider probe base, $880 \times 680 \,\mu\text{m}^2$ and $2440 \times 680 \,\mu\text{m}^2$ in size for the 1D and 2D arrays, respectively, carrying bonding pads used to interconnect the probe to the external instrumentation.

In contrast to the passive NeuroProbes arrays, with one bonding pad per electrode,[17] only 13 or 44
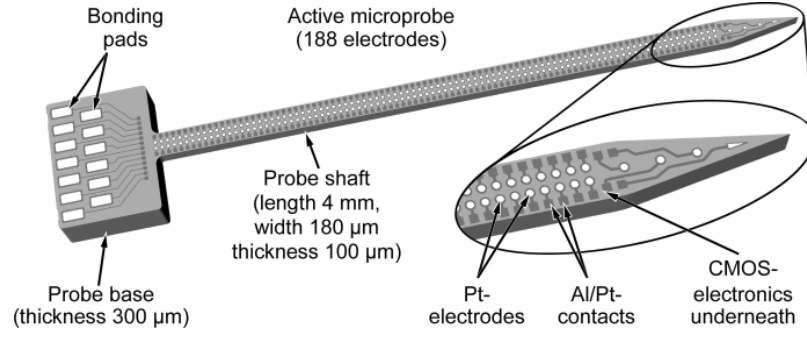
Fig. 1. Schematic of a single-shaft EDC probe comprising CMOS-based electronics interfacing the platinum electrodes arranged in two columns of 92 electrodes along the probe shaft, in addition to four electrodes at the probe tip, adapted from Ref. 4. The probe is connected either to a PCB or a flexible ribbon cable using 13 bonding pads $60 \times 130 \, \mu\text{m}^2$ in size.

bonding pads are required for the 188 or 752 electrodes on the single-shaft probes or four-shaft probe combs of the EDC probes. This reduced number of bonding pads is enabled by a CMOS-based switch matrix integrated directly on the probe shaft underneath the electrode array (Fig. 2(a)), as originally proposed in Ref. 13, and detailed elsewhere.[4]

The switch matrix is based on transmission gates controlled by D-type flip-flops (D-FF)[19] and used to connect the electrodes to analogue output lines (Fig. 2(b)). As highlighted by the gray rectangle in Fig. 2(a), sets of four electrodes with two switches per electrode, i.e. represented as open circles in Fig. 2(a), are combined to elementary cells (EC_i) comprising eight output lines A_i ($i = 1..8$). Within these elementary cells, each electrode is switchable to two out of the eight output lines, e.g. electrode E_1 can be connected either to output lines A_1 or A_3, while electrode E_3 is assigned to the output lines A_5 and A_7. The entire switch matrix on the probe shaft is realized by connecting multiple copies of these EC in series, enabling switch matrices of any length to be generated. As illustrated in Fig. 2(a), the probe layout with 188 electrodes along the 4-mm-long probe shafts requests 46 ECs in addition to a reduced elementary cell rEC with four possible output lines only. The rEC connects the four tip electrodes to one output line each. This concept of a switch matrix enables to select any combination of two tetrodes T_i ($i = 1, 2$), i.e. 2×2 arrays of adjacent electrodes $\{E_1/E_2/E_3/E_4\}$. Examples are tetrodes $T_1 = \{EC_n - E_1/EC_n - E_2/EC_n - E_3/EC_n - E_4\}$ and $T_2 = \{EC_m - E_1/EC_m - E_2/EC_m - E_3/EC_m - E_4\}$ or $T_1 = \{EC_n - E_2/EC_n - E_4/EC_{n+1} - E_1/EC_{n+1} - E_3\}$

and $T_2 = \{EC_m - E_2/EC_m - E_4/EC_{m+1} - E_1/ EC_{m+1} - E_3\}$ with $m \neq n$. However, as soon as two electrodes of the same number located in different ECs are selected, e.g. electrodes $EC_n - E_2$ and $EC_m - E_2$ (with $m \neq n$) connected to the output lines A_2 and A_4, respectively, no additional electrode E_2 within a third EC can be selected. Consequently, not all electrode combinations of eight individual electrodes along the probe shaft are possible in contrast to the tetrode combinations.

The output lines A_1 through A_8 of the switch matrix are accessible at corresponding bonding pads on the probe base and might be interfaced with any multi-channel recording system. The remaining five and twelve bonding pads on the probe base of the 1D and 2D probe arrays, respectively, are used as input lines to control the EDC probe, i.e. power supply, i.e. V_{SS}, V_{DD} and CLOCK, and digital lines DIN and DOUT for electrode selection and control (Fig. 2(b)).

The access to eight analogue output lines is limited due to the applied $0.6 \, \mu\text{m}$ CMOS fabrication technology used to realize the integrated switch matrix. With a typical size of the switch matrix transmission gates of $40 \times 30 \, \mu\text{m}^2$ including the corresponding D-type flip-flops,[19] and the request to keep the probe shaft width as narrow as possible in order to minimize tissue trauma, the number of switching units per EC had to be limited to 16. Based on this limitation, a probe shaft width of $180 \, \mu\text{m}$ at an electrode pitch of ca. $40 \, \mu\text{m}$ was feasible. The second factor limiting the number of output lines was compatibility of the 2D probe combs with the 3D probe array concept, as introduced in Refs. 20 and 21. In this case, the probe comb base comprises four
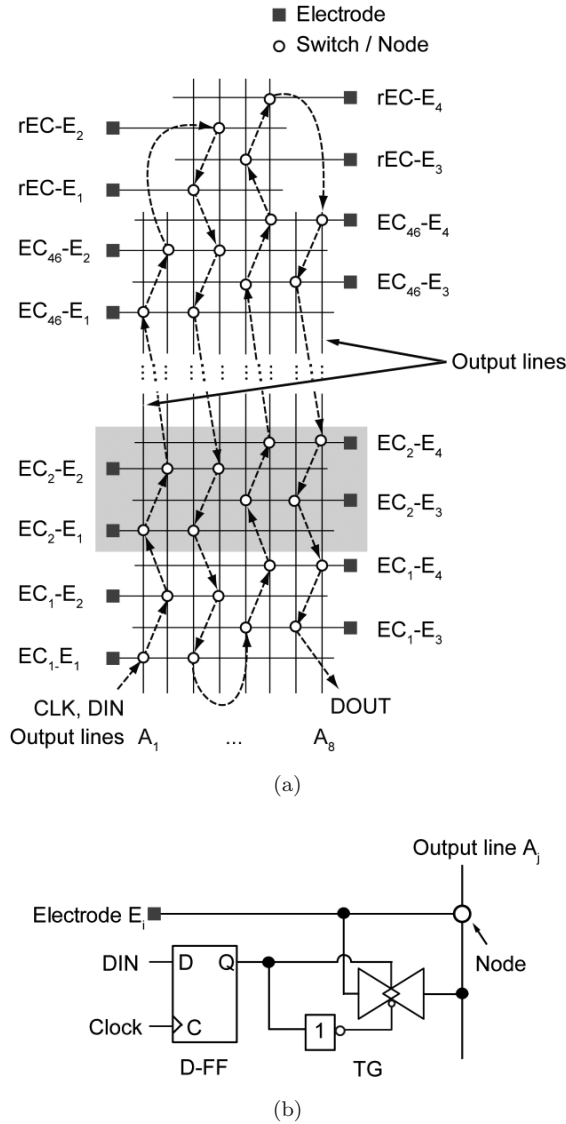
Fig. 2. (a) Schematic representation of the switch matrix integrated along one probe shaft (adapted from Ref. 19). The elementary cell (EC) of the switch matrix comprising four electrodes and eight switches is highlighted by the gray rectangle. (b) Schematic of a single node consisting of a transmission gate controlled by a D-FF to connect an electrode to a specific output line.

base segments assembled into corresponding cavities in a MEMS (micro-electro-mechanical systems) platform.[6]

The probe array is reconfigured using a clock frequency of 1 MHz corresponding to a reconfiguration time of $372\,\mu s$ per shaft. An additional relaxation time of about $500\,\mu s$ is required due to time constant determined by the electrode resistance and capacitive loads. Therefore, fast multiplexing between all

electrodes is prevented and might require additional buffers before multiplexing. However, static access to a large amount of electrodes with a high local resolution is a great technological advance and not possible with passive probe arrays.

The fabrication of the probe arrays is based on a commercial $0.6\,\mu m$ CMOS technology, i.e. process XC06 from X-FAB Semiconductor Foundries AG, Erfurt, Germany, used to realize the integrated circuitry and a post-CMOS MEMS (micro-electro-mechanical systems) process applied to deposit, pattern and passivate the biocompatible Pt metallization of the electrodes and to define the probe geometry using deep reactive ion etching of silicon. Fig. 3 shows an optical micrograph of a probe comb and two single-shaft probes suspended in the fabrication wafer and scanning electron microscopy images of a section of the probe shaft with two columns of electrodes.

Further details on the integrated switch matrix, the probe operation and the applied fabrication process are described elsewhere.[19] Experimental *in vivo* recordings performed in the rat cortex using active EDC probe arrays are described elsewhere.[22] Probes
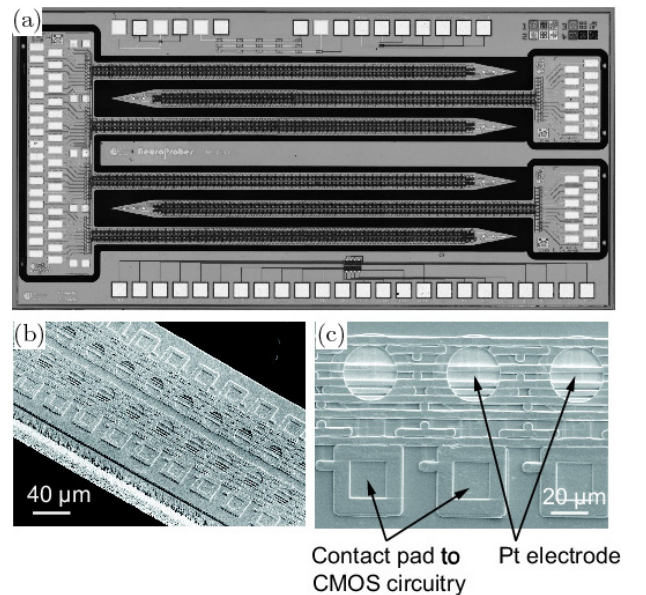

Fig. 3. (a) Optical micrograph of an EDC probe comb and two single-shaft probes suspended within the fabrication wafer. (b) Scanning-electron-microscopy image of a section of the probe shaft with the two columns of electrodes. (c) Details of the circular electrodes connected to the quadratic contact pads of the CMOS electronic. The optical micrograph is adapted from Ref. 18.

of similar architecture with a length of 8 mm realized using a different CMOS process are described in Ref. 6, demonstrating the capability of these probes to record simultaneously from the sensory cortex and the thalamus in the rat.

2.2. *Neural model*

2.2.1. *Network structure and motivation*

The neural model was designed to generate ground-truth data with which the analysis of high-density electrode recordings could be validated. The data can be used for testing algorithms for the *in vivo* sorting of spikes and for the detection of synchronization between neurons recorded on different shafts or probes. In the present paper, only local signals captured on a single-shaft probe are considered. The organization of the generic model was motivated by the following two requirements.

Firstly, the model should provide realistic extracellular potentials and a variety of realistic spike shapes. Since extracellular potentials are also generated by synaptic currents,[23] it was more expedient to model a few neurons with realistic dendrites, rather than having a large population of primitive neurons. Secondly, in order to test for fleeting synchronization between different columns, each column should have intrinsic dynamics. This was generated in the model,

in spite of the sparsity of its neurons, through populations of intra- and inter-columnar feedback fibers that had their spike rates modulated by representative neurons of each column (see further). For the purpose of the present paper, which studied signals on a single shaft, only a single column of five neurons was simulated. This model is nevertheless far more realistic in simulating extracellular potentials compared to previous research[7] which used only two identical pyramidal cells to simulate a mechanical depth control algorithm.

The layout of the electrode configuration, as described in Sec. 2.1, is mapped onto the model in Fig. 4. The present minimal network model contains one layer-5 tufted pyramidal cell, two nontufted pyramidal cells and two inhibitory interneurons (see for instance Ref. 24). The central neuron at position $(0, 0, 0)$ is a tufted pyramidal cell (blue), flanked by a non-tufted pyramidal cell (black) at position $(-40, 0, 200)$ (all coordinates in μm) and an inhibitory interneuron (red) at position $(40, 0, 100)$. Two additional neurons were placed outside the plane of the electrode array: a non-tufted pyramidal cell (green) at $(20, 30, 300)$ and an inhibitory interneuron (yellow) at $(-20, -30, 300)$. As explained below, the network was driven by a population of afferent fibers, providing feedforward excitation and (di-synaptic) inhibition.
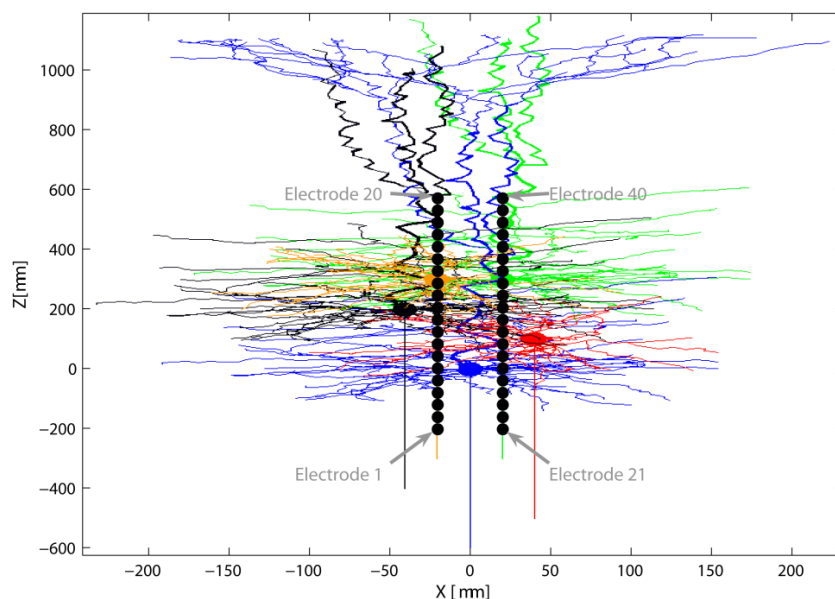

Fig. 4. Part of the electrode configuration on a single shaft as in Fig. 1 mapped onto the five neurons of the network model. See text for details.
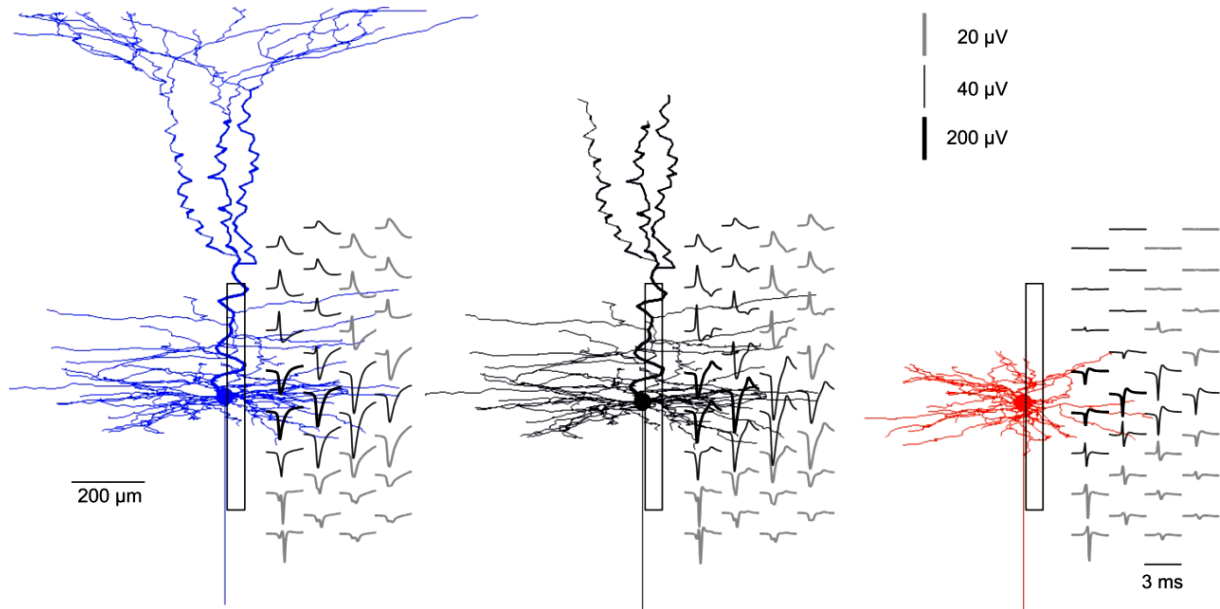
Fig. 5.   The three types of model neurons illustrated separately. Neuron morphologies are depicted in blue and black for the tufted and non-tufted pyramidal cell, and in red for the stellate-shaped inhibitory neuron. The matrix of traces overlaying each neuron depicts the extracellular waveform of the action potential at different positions. These positions were located within a narrow vertical rectangle with coordinates in μm relative to the soma of $(8.7, -210)$ and $(60.6, 210)$; horizontal distance between columns corresponds to $17.3\,\mu$m; vertical distance within a column to $60\,\mu$m. Different vertical scale bars apply to traces with different degrees of grey saturation. Note that the traces were obtained from network simulations in which an electrode array was centred at the particular neuron and allowed to record, for the sake of clarity, only potentials from that neuron.

2.2.2.   Three types of model neurons

Tufted pyramidal cell. The largest model neuron, stretching over the entire depth of the cortex, was a tufted layer-5 pyramidal cell (Fig. 5, blue), reconstructed in Ref. 25. The authors in Ref. 26 segmented its dendrite into 2059 compartments, and provided both dendrite and soma with active ionic channels and a Ca^{2+}-pool, following Ref. 27. We extended and modified this model neuron as follows. Firstly, we added a 600-μm axon, segmented into 20 compartments and with a conduction speed of $0.6\,ms^{-1}$, as described in Ref. 28. Secondly, each dendritic compartment was provided with an excitatory (AMPA receptor) and inhibitory ($GABA_A$ receptor) synapse, the details of which are given in Ref. 29. Note that we did not use the model neuron's NMDA and $GABA_B$ receptors in the present simulations. Thirdly, the excitability of the dendrite was attenuated by decreasing the density of fast Na^{+}-channels, T- and L-type Ca^{2+}-channels and delayed rectifier K^{+}-channels. This attenuation to 30% of

the original model was needed to prevent the dendrite from generating spikes after synaptic stimulation. Note that all cells in the present network were excited in a realistic manner by the activation of hundreds of synapses on their dendrites, unlike those of other studies,[7,26,30,31] which received excitatory current through an electrode inserted into their soma.

Non-tufted pyramidal cell. Cutting the tuft of the pyramidal neuron left a model neuron of 1452 compartments (Fig. 5, black). All ionic channels were similar to those of the tufted cell, except for a further attenuation, to 5% of the original model, of the dendritic excitability.

Stellate-shaped inhibitory interneuron. The lack of detailed interneuron reconstruction data led us to use the basal dendrites of the pyramidal cell as a stellate morphology. The resulting model neuron had 866 compartments (Fig. 5, red), and its membrane channels were borrowed from a previous simulation study of inhibitory networks.[32]
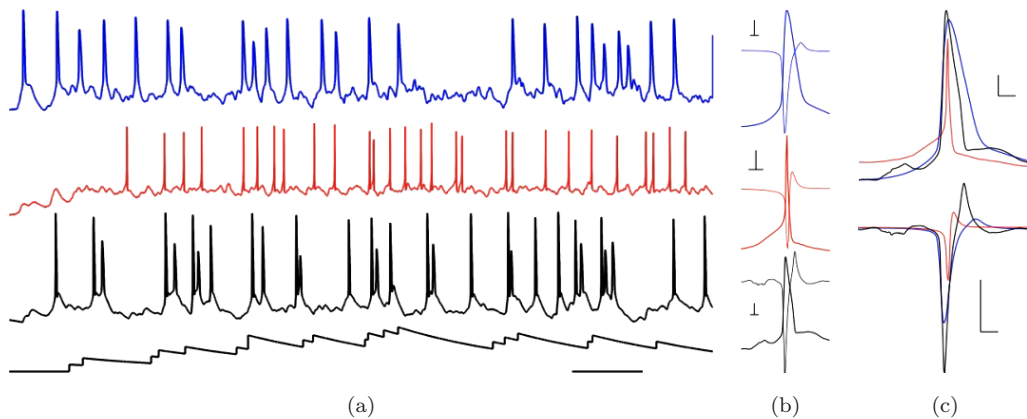
Fig. 6. The three types of neuron generate different spike shapes and discharge patterns. (a) Somatic membrane potential responses of the tufted pyramidal cell (blue), the inhibitory interneuron (red) and the non-tufted bursting pyramidal cell (black) in a 3-neuron network driven by feedforward afferent fibers. The bottom trace plots the modulation of the instantaneous spike rate of the afferent fibers. Unequal spike heights are partly a 20-kHz-sampling artefact, but the pyramidal neurons also exhibited marked amplitude attenuation of their spikes during repeated discharge. (b) Overlaid spike-triggered average membrane potential (vertical scale bar 10 mV) and extracellular potential (same scale bar 0.1 mV) for each of the neuron types. The trigger was an upstroke of the membrane potential crossing the −10 mV level. (c) Same curves as in B, overlaid to highlight differences in spike shape as represented by the membrane potential (top, vertical scale bar 10 mV) or the extracellular potential (bottom, vertical scale bar 0.3 mV). Membrane potentials were measured at the soma compartment; extracellular potentials at a distance of 8.7 μm, level with the soma. Horizontal scale bars 50 ms (a) and 1 ms (b) and (c).

Figure 6 shows the different somatic spike shapes produced by the model. In Figs. 6(b) and 6(c), the spike heights, measured from the beginning of each trace to the peak, measured 77 mV (tufted pyramidal cell), 60 mV (inhibitory interneuron) and 81 mV (non-tufted pyramidal cell). The respective full widths at half height were 1.6 ms, 0.2 ms and 1.0 ms. The non-tufted pyramidal cell tended to fire in bursts (Fig. 6(a)), and both pyramidal neurons showed marked adaptation of their spike height (see below). Note however that also amplitude-attenuated spikes produced full-height spikes at the axon, where they were boosted by the high density of Na$^+$-channels (not shown).

2.2.3. *Six populations of afferent fibers*

The network received excitatory and inhibitory inputs generated by two populations of afferents, each counting 2058 fibers. Both the excitatory and the inhibitory populations were further subdivided into three pools, 686 fibers each, providing either feedforward connections, or intra-columnar and inter-columnar feedback connections (the latter not being used in the present simulation). For reasons of economy, these pools were generated as

follows. With each dendritic compartment of the tufted layer-5 pyramidal cell, 2058 in total, an excitatory and an inhibitory fiber were associated and pseudo-randomly assigned to one of the three sub-pools. Both fibers were positioned at the same depth as the compartment, and allowed to make connections to all compartments within the same horizontal plane.

Each of the fibers was a Poisson point process, with its instantaneous rate modulated according to the type of fiber (Fig. 7). More precisely, all feedforward afferent spikes were generated by a doubly stochastic process, as in Ref. 33. A single Poisson point process, shared by all feedforward fibers, produced events that were filtered with an exponentially decaying impulse response of 100-ms time-constant (boxed trace in Fig. 7). The resulting signal (see also bottom trace in Fig. 6(a)) was then used to set the instantaneous spike rate of each feedforward fiber. The spikes of inhibitory feedforward fibers were delayed by 1 ms to account for the disynaptic nature of inhibition evoked by subcortical stimulation. The instantaneous spike rate of the excitatory and inhibitory intracolumnar feedback fibers were set using the membrane potentials of the tufted pyramidal neuron and the inhibitory interneuron
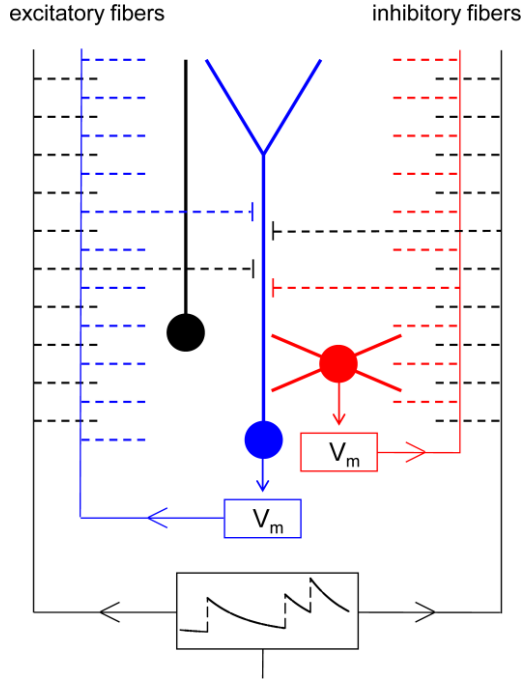
Fig. 7. Organization of core neurons and fibers in the model (see text for details). Vertical (see boxed trace) and horizontal dashed line segments (fibers) represent nonstationary Poisson point processes. The membrane potential (Vm) of the tufted pyramidal cell (blue) is used to set the instantaneous rate of 686 excitatory intracolumnar feedback fibers (blue dashed line segments). Similarly, the membrane potential (Vm) of the inhibitory interneuron (red) is used to set the instantaneous rate of 686 inhibitory intracolumnar feedback fibers (red dashed line segments). The instantaneous rate of 686 excitatory and 686 inhibitory subcortical feedforward fibers (black dashed line segments) is set by an independent Poisson process convolved with a decaying exponential (boxed trace). Note that the membrane potential of the non-tufted pyramidal cell (black) can be used to set the rate of the intercolumnar feedback fibers, which were however absent in the present one-column model. Fibers were allowed to make synaptic connections on all neuronal compartments within the same horizontal plane; only four exemplary synapses on the tufted pyramidal cell are shown. The fourth and fifth neuron are omitted for they received only input without providing feedback.

(augmented by 80 mV and with gain 10), respectively. The intercolumnar fibers were not used in the present study. The green and yellow neurons of Fig. 4 did not provide feedback to the network.

2.2.4. *Model implementation*

The network was built with the GENESIS simulation package (http://www.genesis-sim.org). Differential equations were numerically solved using Crank-Nicolson integration in 10-μs steps. Extracellular potentials were calculated and sampled at 20 kHz during 25-s runs.[a]

2.2.5. *Calculation of extracellular potentials*

Extracellular potentials are a consequence of current flow through a resistive medium. The currents are generated by transmembrane channels, and continue their path along a closed circuit through the intra- and extracellular medium. Hence each compartment in the model can be considered a current source or sink.

The membrane potential V (in volts) of each compartment also obeys the current-balance equation, which can be written as:

$$C\frac{dV}{dt} - \sum_i g_i(V)\,(E_i - V) = \sum_j g_j(V_j - V), \quad (1)$$

where C is the membrane capacitance in farads, E_i the reversal potential of an ohmic transmembrane channel in the classic Hodgkin–Huxley parallel-conductance model, g_i the potentially voltage-dependent conductance in siemens of the channel, and V_j the membrane potential of an adjacent compartment that is connected through a passive resistor of conductance g_j. The terms on the left-hand side represent the capacitive component of the membrane current and the ohmic membrane currents (leak, voltage-gated, ligand-gated), and those on the right-hand side the intracellular axial currents from and to other compartments (commonly one upstream and one downstream, and an additional one at a bifurcation of the dendritic tree). Hence, the total transmembrane current is easily calculated from the sum of the passive axial currents.

Each compartment, being regarded as a point current source of magnitude i_o (in ampères), has its contribution to the extracellular potential at a point at distance r as $i_0/(4\pi\sigma_0 r)$, with σ_0 the tissue conductivity set to $0.25\,\mathrm{S\,m^{-1}}$. This formula assumes an infinite, homogeneous medium without capacitive component.

---

[a]All code is available on simple request from the first or the last author.

Figure 5 shows the extracellular potentials generated in the vicinity of each neuron type. Note (1) the reversal of polarity along the depth axis, (2) the rapid fall in amplitude with distance from the soma (potential falls as $1/r$ with distance), (3) the split negative deflections at the level of the axon, caused by the propagation delay which separates the somatic from the axonal action potential.

2.3. *Spike detection*

Spike detection is an important step in the methods of electrode selection to be presented in Secs. 3.2 and 3.3. We discuss here the background on spike detection using the continuous wavelet transform.

The signal, $x^i[t]$, obtained at electrode i consists of a noise-free extracellular potential, $s^i[t]$, distorted by a noise term $n^i[t]$:

$$x^i[t] = s^i[t] + n^i[t], \quad \text{with } t = 0, \ldots, N-1, \quad (2)$$

with N the number of samples. N is equal to 500000, because the model was run for 25 s at 20 kHz sampling rate. The traces of the extracellular potential, $s^i[t]$, were generated by the model at the electrode positions shown in Fig. 4. The noise term originates from various sources[7]: the thermal noise from the recording electrodes, noise from recording hardware, quantization noise due to analogue-to-digital conversion (A/D), and the summed activity of many distant neurons. Due to the difficulty to model all these aspects of the noise, we used actual recordings from the probes in which no spikes could be visually detected (Sec. 2.5). The same methodology of obtaining ground-truth data, in which the noise-free extracellular potentials $s^i[t]$ are simulated, and $n^i[t]$ is obtained from actual noise recordings, was applied in Ref. 7. Before applying spike detection, we filtered the signals $x^i[t]$ using an elliptic bandpass filter (4th order, 300 Hz and 3000 Hz cut-off frequencies, 0.01 dB of peak-to-peak ripple and a minimum stopband attenuation of 60 dB). Non-causal filtering (command filtfilt in MATLAB$^\circledR$) was applied to minimize spike shape distortion.[34]

We used the continuous wavelet transform to perform spike detection, the reader is referred to Ref. 35 for details on the following paragraph. After taking the inner product of $x^i[t]$ and the wavelet functions $\psi_{j,k}[t]$, the wavelet coefficients at electrode i, scale j

and time k are:

$$X^i(j,k) = \langle x^i, \psi_{j,k} \rangle. \quad (3)$$

The absolute value of $X^i(j,k)$ is used to determine whether a spike may occur at scale j and time k as follows:

$$|X^i(j,k)| > \frac{\hat{\mu}_j^i}{2} + \frac{(\hat{\sigma}_j^i)^2}{\hat{\mu}_j^i} \ln(\gamma_j). \quad (4)$$

All time stamps k for which the absolute value exceeds the threshold are considered as candidate spike stamps. Here $\hat{\mu}_j^i$ is an estimate of the mean amplitude of coefficients $|X^i(j,k)|$ over all k's at which spikes are roughly assumed to occur, i.e. at all k's for which $|X^i(j,k)| \geq \hat{\sigma}_j^i \sqrt{2\ln(N)}$, and $\hat{\sigma}_j^i$ is a robust estimator for the noise standard deviation at electrode i and scale j. The threshold value γ_j can be chosen as a function of the ratio of the cost of false alarms (a spike is detected, but no spike is present) and the cost of omissions (a spike is present but is not detected). We performed experiments with this ratio equal to 1 (the cost of an omission and the cost of a false alarm are considered to be equal). This value can be considered as a default setting.[35] The median absolute deviation (MAD) is used as a robust estimator for the standard deviation:

$$\hat{\sigma}_j^i = \text{median}(|X^i(j,0) - \bar{X}^i(j,.)|, |X^i(j,1) \\ - \bar{X}^i(j,.)|, \ldots |X^i(j,N-1) - \bar{X}^i(j,.)|)/0.6745, \quad (5)$$

with $\bar{X}^i(j,.) = (1/N) \sum_{k=0}^{N-1} X^i(j,k)$ the time average at scale j. The wavelet coefficients over different neighbouring scales are combined to determine the exact occurrence of the spikes.[35]

The time scales in the continuous wavelet transform were selected to detect events of a full width between 0.5 and 1.5 ms. Hence, the duration of an extracellular spike was expected to be about 0.5 ms minimally and about 1.5 ms maximally. This broad range of spike durations was needed in order to capture both pyramidal cells and interneurons. Indeed interneurons have a shorter spike duration compared to pyramidal cells.[36] The developed neural model was able to replicate this behaviour (see Fig. 8). We used the Daubechies 2 (db2) mother wavelet function, but other wavelets such as the Haar wavelet and wavelets from the biorthogonal family can also be used.[35]
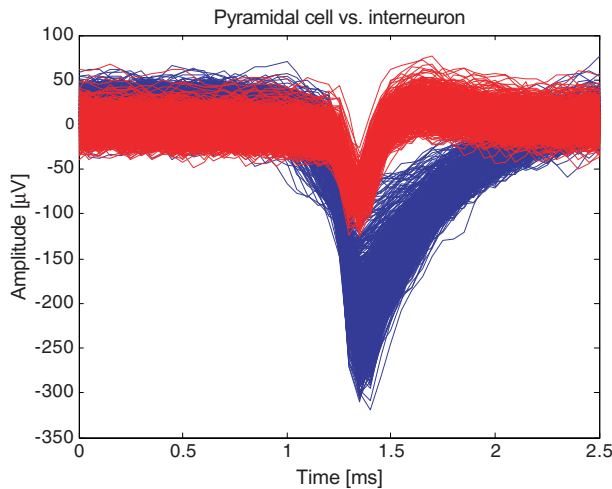
Fig. 8. Spike waveforms detected by the algorithm from noise-added extracellular potentials generated by the model. Spikes of the tufted pyramidal cell (blue) are captured on electrode 6; those of the interneuron (red) on electrode 28, following the electrode lay-out in Fig. 4. The large variation of spike amplitude for the pyramidal cell was attributed to an ISI (inter-spike interval) dependent amplitude attenuation.

2.4. *Spike sorting*

Spike sorting methods can be divided into two main categories[2,37]: (1) spike sorting based on waveform similarity in a signal recorded with a given electrode and (2) spike sorting by exploiting that nearby neurons, when recorded from by different electrodes, will possess different spike amplitudes (called triangulation). The first category consists in assigning spikes with similar waveforms to the same cluster and associate each cluster with a different neuron, multi-unit or noise. In Sec. 3.1 we will show the weakness of this method for classifying spikes generated by the model. Note that due to the large number of electrodes in high-density electrode arrays, manual spike sorting is no longer feasible. Moreover the results of manual spike sorting are highly subjective: subjects often disagree on whether a signal constitutes a spike versus noise as well as on the number of units present in the data.[38] In particular, subjects tend to oversegment channels in which only one neuron is present.

Among the most popular clustering techniques for automated spike sorting in the first category are the ones based on Gaussian mixture models.[39–41] In Ref. 42 the authors proposed a robust extension of Gaussian mixture models by using mixtures of t-distributions. An appealing property of that

algorithm is that it allows to perform spike sorting in an automatic way, in particular no user-intervention is required to determine the number of neurons recorded. This was achieved by using an information-theoretic criterion, the minimum message length (MML), as originally proposed in Ref. 43 for the Gaussian mixture model, which penalizes the goodness-of-fit of a mixture model with the complexity of that model.

2.5. *Noise recordings*

The noise recordings, as required in Eq. (2), were obtained in the somatosensory cortex of anaesthetized rats, sampled at 20 kHz (courtesy of István Ulbert). The signals were pre-filtered with a 4th-order Bessel analogue 0.1 Hz high-pass filter and a 4th-order Bessel analogue 5000 Hz low-pass filter.

3. Results and Discussion

We first demonstrate the inadequacy of classical spike sorting for the identification of single units in the developed model (Sec. 3.1). Then we show, in Sec. 3.2, that electrode selection based on the raw signal-to-noise ratio fails to capture small-amplitude spikes. Finally, we present, in Sec. 3.3, an improved method based on the penalization of electrodes that detect spikes already captured on other electrodes.

3.1. *Classical methods for spike sorting misclassify amplitude-attenuated spikes*

We applied robust, automatic spike sorting, using the multi-variate t-mixture model, to some single-unit channels after PCA (principal component analysis) had been applied to the spike waveforms. The expectation-maximization algorithm was run several times with the mean vectors initialized by drawing at random 10 data points from the two-dimensional principal-component space. Figure 9 shows the clustering in which the minimum message length over the different runs was obtained for a segmentation in two clusters. Clearly, the mixture of t-distributions is confused by the spike amplitude variability. The model separated the action potentials from a single neuron (the tufted pyramidal model neuron) as if they were emitted by two neurons: one cluster captures the smaller spike amplitudes, whereas the
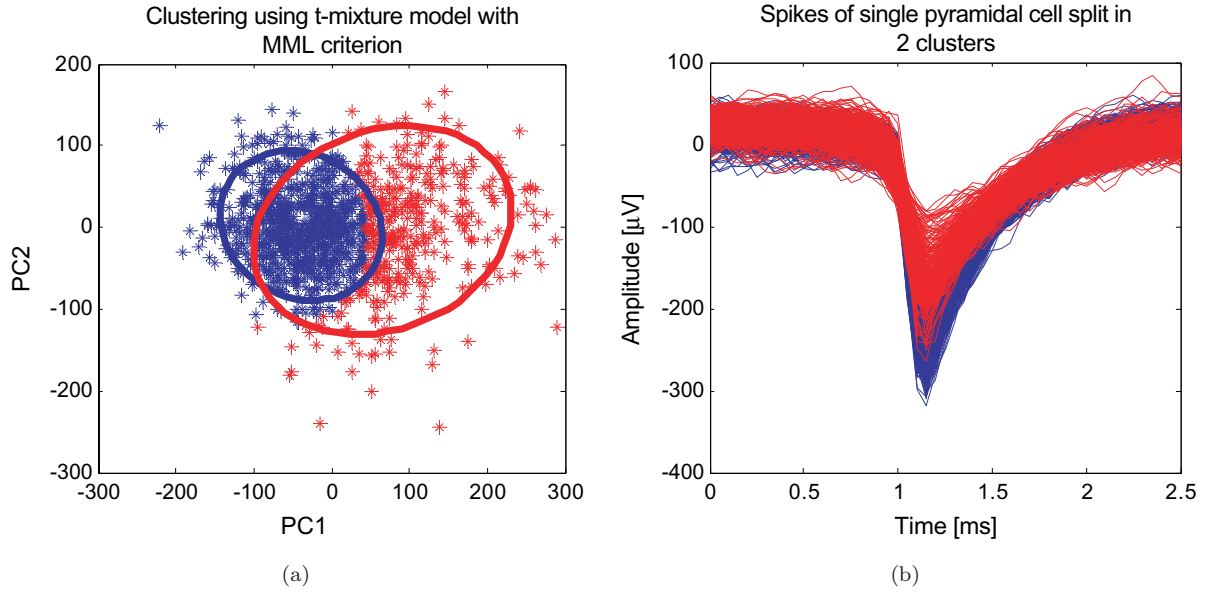
Fig. 9.   Spike sorting of the single neuron that was captured on electrode 6 (blue neuron, see Fig. 4). The single neuron is split in two clusters (a) by a multi-variate t-mixture model when minimizing the message length (MML). Ellipses represent two times the covariance matrix. The degrees of freedom, ν, obtained after training the parameters is equal to 42.23. The prior probabilities, π_1 and π_2, for the two clusters are equal to 0.627 (blue) and 0.373 (red). At electrode 6 the spikes of the other neurons are negligible. (b) The red cluster captures the smaller amplitude attenuated spikes whereas the blue cluster captures the larger spikes.

other cluster captures the larger-amplitude spikes of the same neuron (Fig. 9(b)). Indeed, spike misclassification due to amplitude attenuation has been observed previously.[44] The waveform variability is a function of the immediate firing history and has been attributed to Na^+-channel inactivation.[45–48] The amplitude and waveform variability of extracellularly recorded spikes are the major cause of errors in spike sorting.[2] Amplitude attenuation is most evident during bursts (inter-spike interval <10 ms following the convention of Ref. 49), as shown in Fig. 10 for the tufted pyramidal model neuron. An exponential model, proposed in Ref. 50, was fitted to the data pairs of spike amplitude versus ISI (inter-spike interval) as follows:

$$\text{Amplitude(ISI)} = A \cdot [1 - \delta \cdot \exp(-\lambda \cdot \text{ISI})]. \quad (6)$$

The resulting parameter values were $A = 233.5$, $\delta = 2.82$, $\lambda = 0.2566$. We used the peak amplitude in Eq. (6). In Fig. 9(b), these peak amplitudes vary between $-100\,\mu\text{V}$ and $-300\,\mu\text{V}$. According to this model the spike amplitude is reduced by 22% at an ISI of 10 ms. At an ISI of 5 ms the amplitude is reduced by as much as 78%. We applied spike sorting also to other electrodes on which we verified visually

that only one neuron was captured. The spikes of a single neuron were, in almost all cases, segmented as if belonging to different neurons. This illustrates the difficulty of traditional spike sorting methods in coping with such complex neuronal data generated by our model.

3.2. Electrode selection using the signal-to-noise ratio (SNR) fails to detect small spikes

A suitable criterion could be employed in order to select those electrodes that are closest to a neuron. So far, the SNR (signal-to-noise ratio) has been used as quality metric to position single electrodes in mechanical electrode positioning systems.[10–12] Spikes recorded close to the soma of a neuron, in particular the axon hillock and the initial segment, have a large amplitude compared to those recorded far from the soma (see Fig. 5 for the model neurons). Larger spike amplitudes result in a larger SNR. Therefore, a selection of electrodes according to the SNR will result in the selection of those electrodes that are likely to be closest to the somata. This fact has been exploited in the mechanical adjustment of the electrode position.[7]
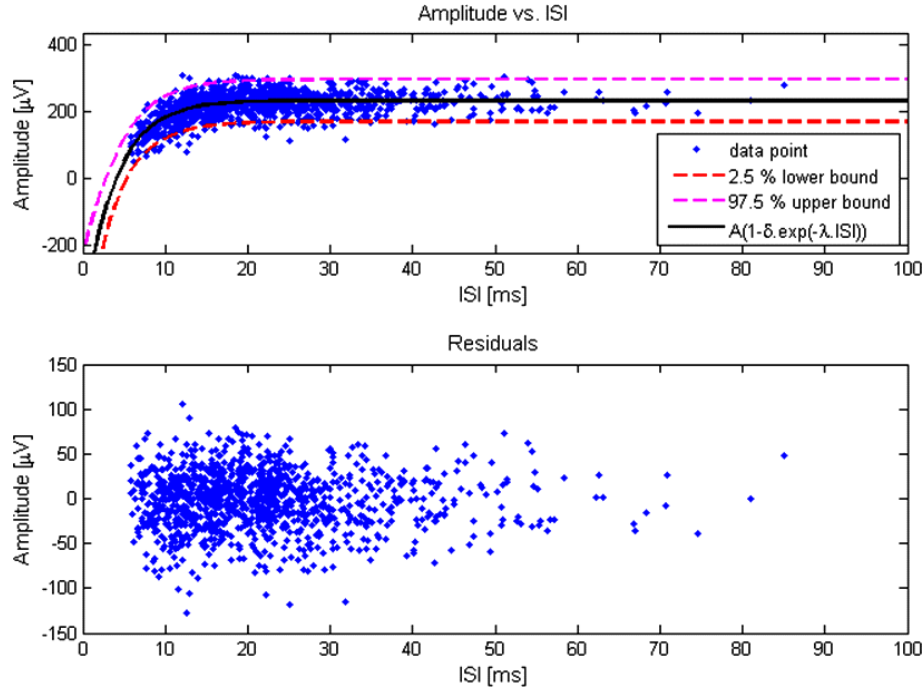
Fig. 10. The variability in spike amplitude can be attributed to ISI-dependent amplitude attenuation. The curves show the model (see text, Eq. (6)) fitted to the data (diamonds). The data were derived from spikes of the tufted pyramidal cell captured on electrode 6 in Fig. 4. The lower panel shows the residuals after fitting.

The SNR is computed as a ratio of the ensemble average of the RMS (root-mean-square) value of the spikes and the standard deviation of the noise:

$$\mathrm{SNR}_{\mathrm{dB}} = 20 \cdot \log_{10} \frac{\frac{1}{N} \sum_{n=1}^{N} \mathrm{RMS}(\mathrm{spike}_n(t))}{\hat{\sigma}_{\mathrm{noise}}}. \quad (7)$$

Here $\mathrm{RMS}(\mathrm{spike}_n(t))$ is the root-mean-square value of spike n computed in a window centred at the spike, and $\hat{\sigma}_{\mathrm{noise}}$ is the MAD estimate of the standard deviation from the noise segments, i.e. parts of the signal outside the windows in which spikes are located. The RMS value was estimated in 2-ms windows centred at the spike (see Fig. 11).

Figure 12 shows the resulting selection of electrodes in descending order of their SNR, taking into account the constraint that in each column up to four electrodes can be selected and that not all combinations of four electrodes on a single column are possible, as explained previously in Sec. 2.1. Note that all eight selected electrodes in Fig. 12 can be read out simultaneously on the eight output lines A_i ($i = 1, \ldots, 8$) (cfr. Fig. 2(a)). Indeed, the first selected electrode can be switched to output line A_1, and the others (in descending order of their SNR) to output lines A_2, A_6, A_5, A_8, A_4, A_7 and A_3.
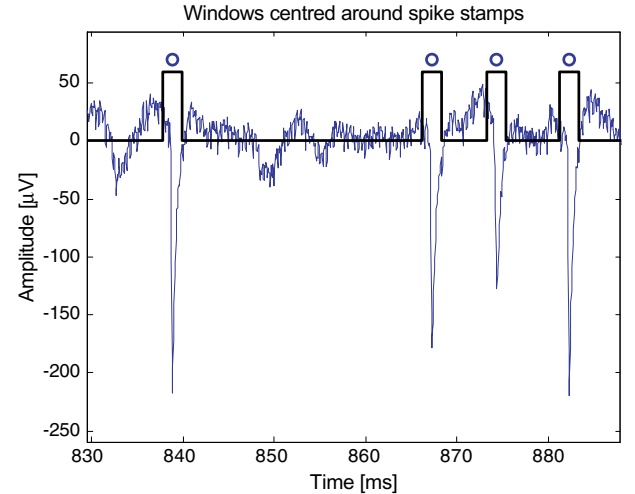

Fig. 11. Windows of 2-ms width centred at the time stamps (circles) of spikes detected for the tufted pyramidal cell.

Figure 13 shows an example trace of the extracellular potential at the selected electrodes. Due to the dense configuration of electrodes on a single shaft, selection according to SNR results in the same neurons being selected multiple times on different nearby electrodes.
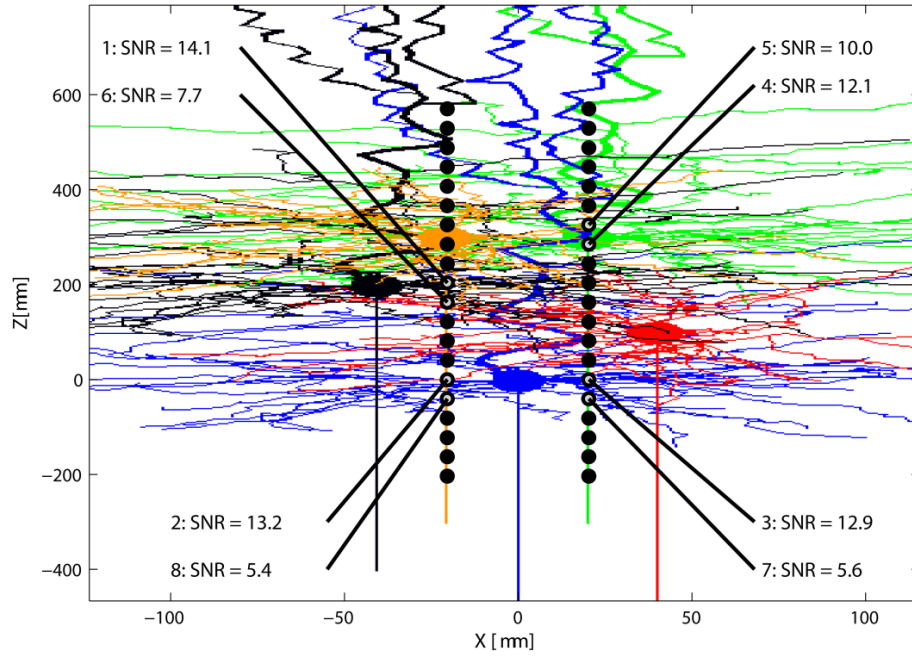
Fig. 12. The selection of eight electrodes using the SNR as criterion. The numbers indicate the order in which the electrodes are selected followed by their SNR values. The black neuron is selected twice (as the 1st and 6th), the blue neuron four times (2nd, 3rd, 7th and 8th), the green neuron twice (4th and 5th). The red and the yellow neuron were not captured.

This leads to the omission of neurons with a lower SNR, for instance the red and the yellow inhibitory inter-neurons which failed to be captured (Figs. 12 and 13). However, the spikes of the selected neurons can be accurately detected on the different channels, as confirmed by the high probability of detection (PD) and low probability of false alarms (PFA) in spike detection (see Table 1). Note that on all channels almost all spikes of a single neuron are found, because the PD is always close to 1. Furthermore, the very few false positives (PFA is always close to 0) indicate that the channels record single-unit activity.

3.3. *Electrode selection using a penalized signal-to-noise ratio (PSNR) selects all neurons of the network*

In order to prevent some neurons from being recorded multiple times while others remain uncaptured, we consider an adjusted metric that not only takes the SNR into account, but also the coincidence of time stamps on different electrodes. If the candidate electrode for selection contains a spike train similar to one on any of the previously selected

electrodes, the electrode should be demoted. In order to achieve this objective, we propose to penalize a candidate electrode, say E_i, as follows:

$$\mathrm{PSNR}(E_i) = \mathrm{SNR}(E_i)$$
$$\cdot \left(1 - \max_{j \in S}(\mathrm{similarity}(E_i, E_j))\right). \quad (8)$$

Here, **S** is the set of already selected electrodes, and similarity (E_i, E_j) is a metric of the similarity between spike trains captured on electrodes E_i and E_j, normalized between zero and one. Hence, in Eq. (8), the $\mathrm{SNR}(E_i)$ is decreased in proportion to the similarity with the most similar already selected electrode. If none of the already selected electrodes contains a similar spike train, the $\mathrm{SNR}(E_i)$ will not be decreased, or only slightly due to a degree of similarity by chance. The similarity between spike trains can be measured by several spike train (dis-) similarity measures. We tested some of the most popular ones[51]: van Rossum spike train metric,[52] Schreiber similarity measure,[53] Hunter-Milton similarity measure[54] and event synchronization.[55] All similarity metrics depend on a time-constant τ. This time-constant determines how close spikes from
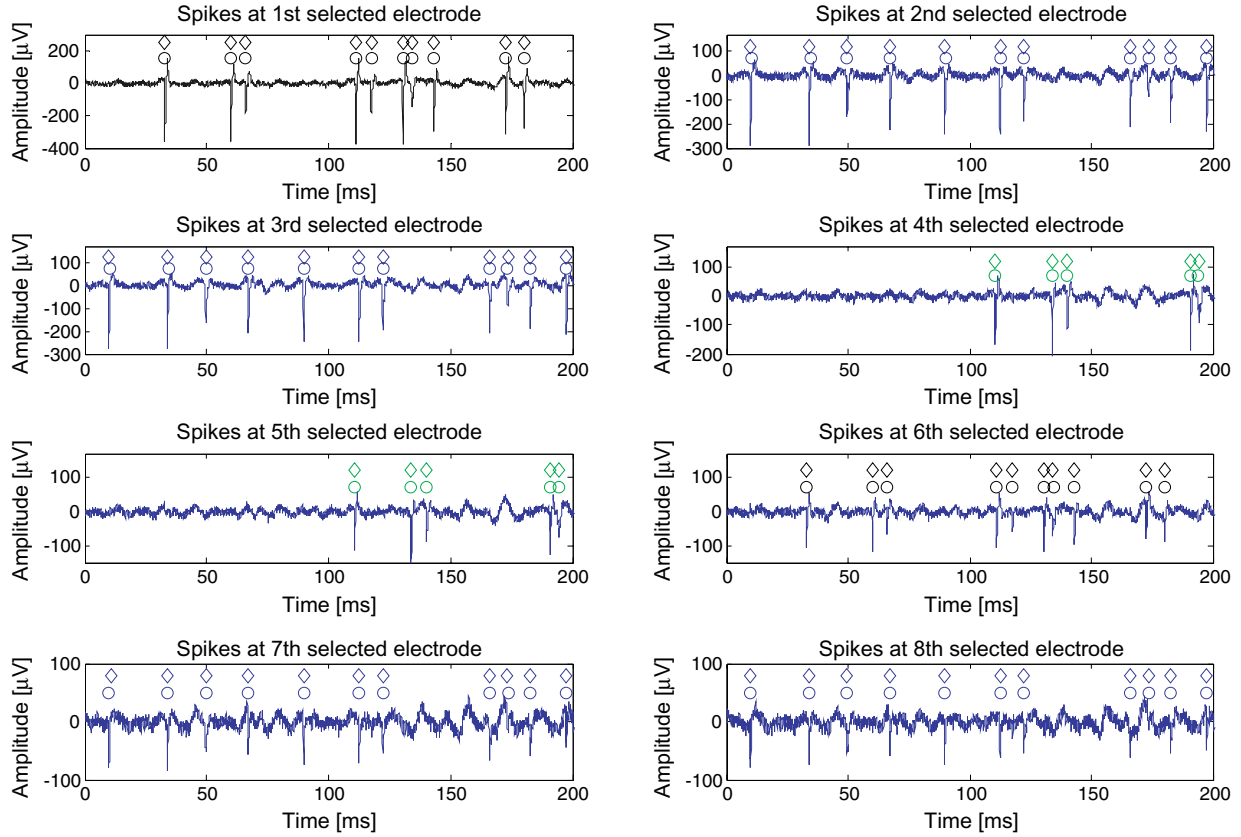
Fig. 13.   Extracellular potentials generated by the five-neuron network model (with added noise), simultaneously recorded by the eight selected electrodes from Fig. 12. Diamonds indicate the true time stamps of the action potentials, which are exactly known from the membrane potentials of the model neurons. Circles are spike time stamps extracted after applying the continuous wavelet transform to the extracellular potential. The colour of the symbols refers to the neuron that emitted the spikes, following the colour code of Fig. 4. The signals on all selected electrodes consist of single-unit activity.

Table 1.   Probability of detection (PD) and probability of false alarms (PFA) for spike detection at the selected electrodes. The PD and the PFA values apply to the target neuron shown in the last column.

Selected electrode	PD	PFA	Target neuron
1st: electrode 11	1	0.0166	Black
2nd: electrode 6	0.9983	0.0431	Blue
3rd: electrode 26	1	0.0269	Blue
4th: electrode 33	1	0.0133	Green
5th: electrode 34	0.9986	0.0173	Green
6th: electrode 10	0.9981	0.0265	Black
7th: electrode 25	0.9974	0.0286	Blue
8th: electrode 5	0.9957	0.0400	Blue

different spike trains should be, in order to contribute to the similarity index. The value of τ was set to 1 ms, so that only spikes on different electrodes that fall in close vicinity of each other contribute to the similarity. This value allows small differences in the exact time stamps of the same action potential on different electrodes to become penalized. Indeed, there may be some jitter between the time stamps assigned to the same action potential by different electrodes, due to noise and differences in spike waveform. The Schreiber spike train similarity metric is computed as follows. Suppose that the time stamps of the spikes on electrode E_i are defined by $\{t_1^i, t_2^i, \ldots, t_{Ni}^i\}$ and those on electrode E_j by $\{t_1^j, t_2^j, \ldots, t_{Nj}^j\}$. Each spike train is convolved with a Gaussian filter of standard deviation τ. This leads to two convolved signals $f_i(t)$ and $f_j(t)$ for electrodes E_i and E_j respectively. The Schreiber similarity is then obtained as the normalized inner product:

$$\text{sim}(E_i, E_j) = \frac{\int_0^\infty f_i(t) f_j(t) \cdot dt}{\|f_i(t)\|_2 \|f_j(t)\|_2}. \tag{9}$$
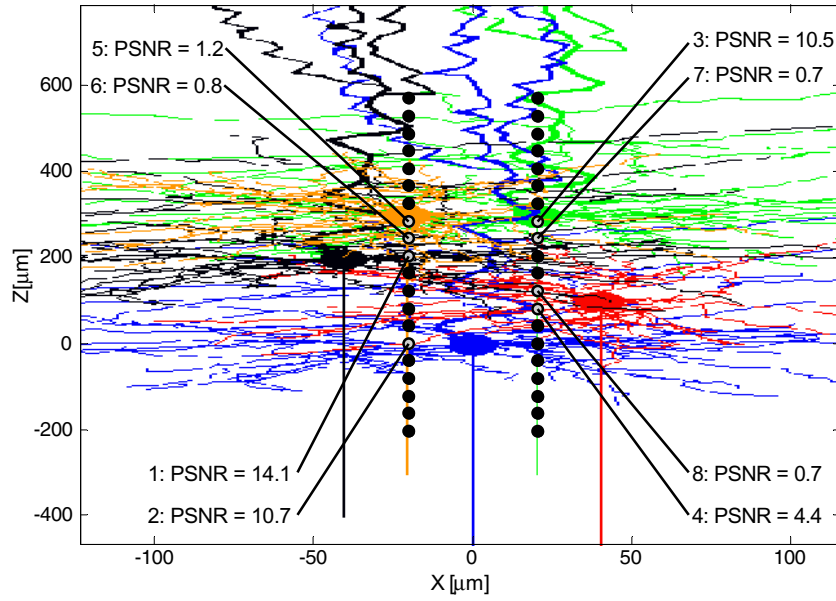
Fig. 14. Selection of eight electrodes using the penalized signal-to-noise ratio (PSNR) as criterion. The numbers indicate the order in which the electrodes are selected followed by the PSNR value. The red neuron is captured on the 4th and 8th electrodes, the yellow neuron is captured on the fifth selected electrode.

Note that a different number of spikes 'Ni' and 'Nj' on the two electrodes is a source of dissimilarity. This is an advantageous property, because it is an indication that the two electrodes record from different neurons.

Applying Eq. (8) iteratively until eight electrodes are selected, using the Schreiber similarity metric of Eq. (9) in Eq. (8), leads to a more efficient selection of electrodes. The first four electrodes selected, using the PSNR selection criterion, now each capture a different neuron, as shown in Fig. 14, whereas in Fig. 12 the blue neuron was selected twice. Moreover, the fifth electrode selected in Fig. 14 now also captures the yellow neuron, although not as single-unit, whereas in Fig. 12 none of the selected electrodes was able to do so. The electrodes selected in Fig. 14 can be switched to the output lines A_i as follows (according to the configuration in Fig. 2(a)): the first selected electrode can be switched to output line A_1, and the others (in decreasing order of their PSNR) to output lines A_2, A_5, A_6, A_3, A_4, A_8 and A_7.

The PD and PFA for the spike detection on the first five channels are shown in Table 2. Note that, as opposed to Table 1, the spikes of the red neuron can now be captured quite accurately: PD = 0.9868 and PFA = 0.1674, see also Fig. 15 left panel. There is, however, a high probability of false alarms

Table 2. Probability of detection (PD) and probability of false alarms (PFA) for the spike detection at the first five selected electrodes. The PD and the PFA are indicated for the target neuron shown in the last column.

Selected electrode	PD	PFA	Target neuron
1st: electrode 11	1	0.0166	Black
2nd: electrode 6	0.9983	0.0431	Blue
3rd: electrode 33	1	0.0146	Green
4th: electrode 28	0.9868	0.1674	Red
5th: electrode 13	0.6981	0.7020	Yellow
5th: electrode 13 with elimination	0.4790	0.3517	Yellow

(PFA = 0.7020) for the yellow neuron on the 5th selected electrode. This is due to the co-recording of spikes from the black and green neurons on that electrode. This problem can be partly resolved by using the information of the spike timings on the electrodes closest to the 5th selected electrode. Indeed, when we eliminate the spikes on the 5th selected electrode that occur at about the same time as the spikes that occur on the 1st and the 3rd selected electrode, the PFA can be drastically decreased to 0.3517, with a relative smaller decrease in PD to 0.4790. To do so, we eliminated all spikes detected at the 5th electrode if they appeared within a 0.5 ms window, to
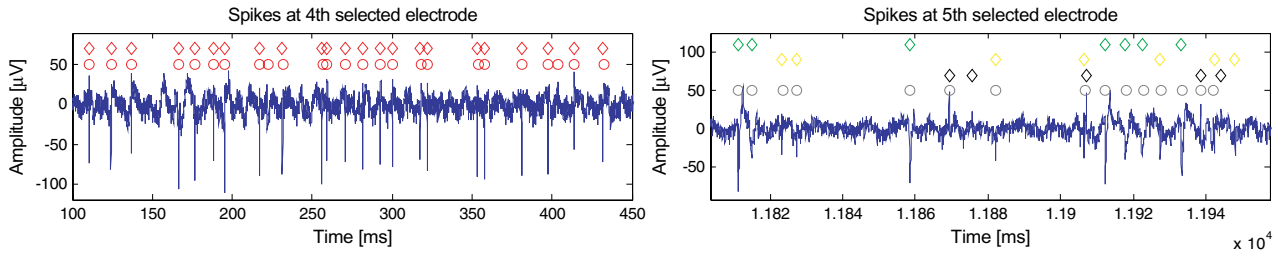
Fig. 15.   With PSNR, neurons can be recorded that were uncaptured with SNR. The spike train on the fourth electrode is single-unit and originates from the red model neuron. The yellow model neuron is captured on the fifth selected electrode, but so are also the green and (sporadically) the black model neuron. As in Fig. 13, diamonds and circles correspond to the actual time stamps (according to the model) and the assigned time stamps (according to spike detection). The detected spikes in the right hand panel are indicated in dark grey.

allow for some jitter in the detection, centred at the spikes detected at the 1st and 3rd electrode. The 2nd and 4th selected electrode were not taken into account as they are more than $200 \, \mu$m away from the 5th selected electrode. It has to be mentioned that the yellow neuron generated extracellular spikes of smaller amplitude (like the red neuron in Fig. 6) and that it is located $30 \, \mu$m out of the plane of the electrodes. This results in very small spike signals that are sometimes indistinguishable from the background noise (see Fig. 15 right panel). Hence, some spikes of the yellow neuron will be missed resulting in a lower PD.

The results of electrode selection (not shown) for the PSNR using the van Rossum spike train similarity metric,[52] the Hunter-Milton similarity measure[53] and event synchronization[55] were the same regardless of the type of similarity metric chosen.

The selection of electrodes with the PSNR may suggest a third way towards spike sorting, exploiting the fact that some units may be simultaneously recorded on different very nearby electrodes. Penalization of such simultaneous recording made the PSNR algorithm select single-unit recordings on four of the selected electrodes. Moreover, units in multi-unit signals may be separated based on their coincident detection by nearby electrodes (as for neuron five in the model). However, the obtained results may depend on the configuration of the neurons, but they seem encouraging enough to warrant further research.

4.   Discussion and Conclusion

The problem of electrode selection bears some similarities with feature selection. In particular, our algorithm has some properties in common with the minimal-redundancy-maximal-relevance algorithm in feature selection.[56] Features are selected according to their relevance, but are demoted if they are redundant with previously selected features. We have tried more complex techniques after PSNR selection of electrodes than the spike elimination indicated in Sec. 3.3. We have applied Independent Component Analysis (ICA) in order to separate the mixed channels into single unit channels.[57] However, this resulted in many single unit channels to become mixed after ICA.

Note that although spiking neural networks[58–62] (SNN) are able to generate spike timings to realistically simulate network dynamics,[63] they do not serve our purpose to create realistic extracellular potentials.

Electronic depth control algorithms aim to select those electrodes, among hundreds of candidates, on high-density electrode arrays, that are close to the neurons' somata. This might be achieved by selecting electrodes with a high signal-to-noise ratio (SNR). However, due to the close spacing of high-density electrode arrays, neighbouring electrodes may capture the same neuron multiple times. In order to be able to select also neurons from which only smaller spikes can be captured such as interneurons, a penalized SNR (PSNR) was introduced. A biologically realistic five-neuron network model was generated that serves to validate electronic depth control algorithms. The neurons are synaptically activated and show realistic spike patterns. We are not aware of any on-line available benchmark models that take spike amplitude attenuation in bursting neurons into account with the purpose to validate spike detection and spike sorting. The current model represents a

single column, but can easily be extended to generate ground-truth data for spike synchronization and for the amplitude or phase synchronization of local field potentials.

Acknowledgements

References

1. E. N. Brown, R. E. Kass and P. P. Mitra, Multiple neural spike train data analysis: State-of-the-art and future challenges, *Nat. Neurosci.* **7**(5) (2004) 456–461.

2. G. Buzsáki, Large-scale recording of neuronal ensembles, *Nat. Neurosci.* **7**(5) (2004) 446–451.

3. J. Pine, A history of MEA development, in *Advances in Network Electrophysiology: Using Multi-Electrode Arrays*, eds. M. Taketani and M. Baudry (Springer, New York, 2006), pp. 3–23.

4. K. Seidl, S. Herwik, Y. Nurcahyo, T. Torfs, M. Keller, M. Schüttler, H. P. Neves, T. Stieglitz, O. Paul and P. Ruther, CMOS-based high-density silicon microprobe array for electronic depth control in neural recording, in *Proc. 22nd IEEE Int. Conf. on Micro Electro Mechanical Systems* (MEMS) (2009), pp. 232–235.

5. K. Seidl, T. Torfs, P. A. De Mazière, G. Van Dijck, R. Csercsa, B. Dombovari, Y. Nurcahyo, H. Ramirez, M. M. Van Hulle, G. A. Orban, O. Paul, I. Ulbert, H. P. Neves and P. Ruther, Control and data acquisition software for high-density CMOS-based microprobe arrays implementing electronic depth control, *Biomed. Tech.* **55**(3) (2010) 183–191.

6. T. Torfs, A. A. A. Aarts, M. A. Erismis, J. Aslam, R. F. Yazicioglu, K. Seidl, S. Herwik, I. Ulbert, B. Dombovári, R. Fiáth, B. P. Kerekes, R. Puers, O. Paul, P. Ruther, C. Van Hoof and H. P. Neves, Two-dimensional multi-channel neural probes with electronic depth control, *IEEE Trans. Biomed. Circuits Syst.*, accepted.

7. Z. Nenadic and J. W. Burdick, A control algorithm for autonomous optimization of extracellular recordings, *IEEE Trans. Biomed. Eng.* **53**(5) (2006) 941–955.

8. L. Grand, L. Wittner, S. Herwik, E. Göthelid, P. Ruther, S. Oscarsson, H. P. Neves, B. Dombovári, R. Csercsa, G. Karmos and I. Ulbert, Short and long term biocompatibility of NeuroProbes silicon probes, *J. Neurosci. Methods* **189**(2) (2010) 216–229.

9. M. S. Fee and A. Leonardo, Miniature motorized microdrive and commutator system for chronic neural recording in small animals, *J. Neurosci. Methods* **112**(2) (2001) 83–94.

10. J. G. Cham, E. A. Branchaud, Z. Nenadic, B. Greger, R. A. Andersen and J. W. Burdick, Semi-chronic motorized microdrive and control algorithm for autonomously isolating and maintaining optimal extracellular action potentials, *J. Neurophysiol.* **93**(1) (2005) 570–579.

11. T. Sato, T. Suzukia and K. Mabuchi, A new multi-electrode array design for chronic neural recording, with independent and automatic hydraulic positioning, *J. Neurosci. Methods* **160**(1) (2007) 45–51.

12. N. Jackson, A. Sridharan, S. Anand, M. Baker, M. Okandan and J. Muthuswamy. Long-term neural recordings using MEMS based movable microelectrodes in the brain, *Front. Neuroeng.* **3**(10) (2010) 1–10.

13. H. P. Neves, T. Torfs, R. F. Yazicioglu, J. Aslam, A. A. A. Aarts, P. Merken, P. Ruther and C. Van Hoof, The NeuroProbes project: A concept for electronic depth control, in *Proc. 30th Annual International Conference of the IEEE Engineering in Medicine and Biology Society* (2008) 1857.

14. H. P. Neves, G. A. Orban, M. Koudelka-Hep and P. Ruther, Development of multifunctional probe arrays for cerebral applications, in *Proc. 3rd Int. IEEE EMBS Conf. on Neural Engineering* (2007) 104–109.

15. P. Ruther, A. Aarts, O. Frey, S. Herwik, S. Kisban, K. Seidl, S. Spieth, A. Schumacher, M. Koudelka-Hep, O. Paul, T. Stieglitz, R. Zengerle and H. P. Neves, The NeuroProbes project — multifunctional probe arrays for neural recording and stimulation, *Biomed. Tech.* **53**(1) (2008) 238–240.

16. H. P. Neves and P. Ruther, The NeuroProbes project, in *Proc. 29th Annual Int. Conf. of the IEEE Engineering in Medicine and Biology Society* (2007) 6442–6444.

17. S. Herwik, S. Kisban, A. A. A. Aarts, K. Seidl, G. Girardeau, K. Benchenane, M. B. Zugaro, S. I. Wiener, O. Paul, H. P. Neves and P. Ruther, Fabrication technology for silicon-based microprobe arrays used in acute and sub-chronic neural recording,

J. Micromech. Microeng. **19**(7) (2009) 074008 (11 pp).

18. P. Ruther, S. Herwik, S. Kisban, K. Seidl and O. Paul, Recent progress in neural probes using silicon MEMS technology, *IEEJ Trans. Electr. Electron. Eng.* **5**(5) (2010) 505–515.

19. K. Seidl, H. Herwik, T. Torfs, H. P. Neves, O. Paul and P. Ruther, CMOS-based high-density silicon microprobe array for electronic depth control in intracortical neural recording, *J. Microelectromech. Syst.* (2011a), accepted.

20. A. A. A. Aarts, H. P. Neves, R. Puers and C. Van Hoof, An interconnect for out-of-plane assembled biomedical probe arrays, *J. Micromech. Microeng.* **18**(6) (2008) 064004 (7 pp).

21. A. A. A. Aarts, H. P. Neves, R. Puers, C. Van Hoof, Recent advances in interconnect technology for slim-base biomedical probe arrays, in *Proc. 15th Int. Conf. on Solid-State Sensors, Actuators & Microsystems* (Transducers) (2009), pp. 1975–1978.

22. K. Seidl, M. Schwaerzle, I. Ulbert, H. P. Neves, O. Paul and P. Ruther, CMOS-based high-density silicon microprobe array for electronic depth control in intracortical neural recording — characterization and application, *J. Microelectromech. Syst.* (2011b), in preparation.

23. A. Viswanathan and R. D. Freeman, Neurometabolic coupling in cerebral cortex reflects synaptic more than spiking activity, *Nat. Neurosci.* **10**(10) (2007) 1308–1312.

24. R. D. Traub, D. Contreras, M. O. Cunningham, H. Murray, F. E. LeBeau, A. Roopun, A. Bibbig, W. B. Wilent, M. J. Higley and M. A. Whittington, Single-column thalamocortical network model exhibiting gamma oscillations, sleep spindles, and epileptogenic bursts, *J Neurophysiol.* **93**(4) (2005) 2194–2232.

25. D. Schubert, J. F. Staiger, N. Cho, R. Kötter, K. Zilles and H. J. Luhmann, Layer-specific intracolumnar and transcolumnar functional connectivity of Layer V pyramidal cells in rat barrel cortex, *J. Neurosci.* **21**(10) (2001) 3580–3592.

26. J. Dyhrfjeld-Johnsen, J. Maier, D. Schubert, J. Staiger, H. J. Luhmann, K. E. Stephan and R. Kötter, CoCoDat: A database system for organizing and selecting quantitative data on single neurons and neuronal microcircuitry, *J. Neurosci. Methods* **141**(2) (2005) 291–308.

27. R. D. Traub, E. H. Buhl, T. Glovell and M. A. Whittington, Fast rhythmic bursting can be induced in layer 2/3 cortical neurons by enhancing persistent Na$^+$ conductance or by blocking BK channels, *J. Neurophysiol.* **89**(2) (2003) 909–921.

28. R. Maex and E. De Schutter, Mechanism of spontaneous and self-sustained oscillations in networks connected through axo-axonal gap junctions, *Eur. J. Neurosci.* **25**(11) (2007) 3347–3358.

29. S. M. Solinas, R. Maex and E. De Schutter, Dendritic amplification of inhibitory postsynaptic potentials in a model Purkinje cell, *Eur. J. Neurosci.* **23**(33) (2006) 1207–1218.

30. G. R. Holt and C. Koch, Electrical interactions via the extracellular potential near cell bodies, *J. Comput. Neurosci.* **6**(2) (1999) 169–184.

31. C. Gold, D. A. Henze, C. Koch and G. Buzsáki, On the origin of the extracellular action potential waveform: A modeling study, *J. Neurophysiol.* **95**(5) (2006) 3113–3128.

32. R. Maex and E. De Schutter, Resonant synchronization in heterogeneous networks of inhibitory neurons, *J. Neurosci.* **23**(33) (2003) 10503–10514.

33. A. Harsch and H. P. C. Robinson, Postsynaptic variability of firing in rat cortical neurons: The roles of input synchronization and synaptic NMDA receptor conductance, *J. Neurosci.* **20**(16) (2000) 6181–6192.

34. R. Q. Quiroga, What is the real shape of extracellular spikes? *J. Neurosci. Methods* **177**(1) (2009) 194–198.

35. Z. Nenadic and J. W. Burdick, Spike detection using the continuous wavelet transform, *IEEE Trans. Biomed. Eng.* **52**(1) (2005) 74–87.

36. J. Csicsvari, H. Hirase, A. Czurko, A. Mamiya and G. Buzsáki, Oscillatory coupling of hippocampal pyramidal cells and interneurons in the behaving rat, *J. Neurosci.* **19**(1) (1999) 274–287.

37. D. R. Kipke, W. Shain, G. Buzsáki, E. Fetz, J. M. Henderson, J. F. Hetke and G. Schalk, Advanced neurotechnologies for chronic neural interfaces: New horizons and clinical opportunities, *J. Neurosci.* **28**(46) (2008) 11830–11838.

38. F. Wood, M. J. Black, C. Vargas-Irwin, M. Fellows and J. P. Donoghue, On the variability of manual spike sorting, *IEEE Trans. Biomed. Eng.* **51**(6) (2004) 912–918.

39. M. S. Lewicki, Bayesian modelling and classification of neural signals, *Neural Comput.* **6**(5) (1994) 1005–1030.

40. M. S. Lewicki, A review of methods for spike sorting: The detection and classification of neural action potentials, *Network* **9**(4) (1998) R53–R78.

41. M. Sahani, J. S. Pezaris and R. A. Andersen, On the separation of signals from neighboring cells in tetrode recordings, in *Advances in Neural Information Processing Systems*, Vol. 10, eds. M. I. Jordan, M. J. Kearns and S. A. Solla (MIT Press, Cambridge, MA, 1998), pp. 222–228.

42. S. Shoham, M. R. Fellows and R. A. Normann, Robust, automatic spike sorting using mixtures of multivariate t-distributions, *J. Neurosci. Methods* **127**(2) (2003) 111–122.

43. M. Figueiredo and A. Jain. Unsupervised learning of finite mixture models, *IEEE Trans. PAMI* **24**(3) (2002) 381–396.

44. K. D. Harris, D. A. Henze, J. Csicsvari, H. Hirase and G. Buzsáki, Accuracy of tetrode spike separation as determined by simultaneous intracellular and extracellular measurements, *J. Neurophysiol.* **84**(1) (2000) 401–414.

45. G. Buzsáki, M. Penttonen, Z. Nádasdy and A. Bragin, Pattern and inhibition-dependent invasion of pyramidal cell dendrites by fast spikes in the hippocampus *in vivo*, *Proc. Natl. Acad. Sci. USA* **93**(18) (1996) 9921–9925.

46. C. M. Colbert, J. C. Magee, D. A. Hoffman and D. Johnston, Slow recovery from inactivation of Na$^+$ channels underlies the activity-dependent attenuation of dendritic action potentials in hippocampal CA1 pyramidal neurons, *J. Neurosci.* **17**(17) (1997) 6512–6521.

47. G. Stuart, N. Spruston, B. Sakmann and M. Häusser, Action potential initiation and backpropagation in neurons of the mammalian CNS, *Trends Neurosci.* **20**(3) (1997) 125–131.

48. K. D. Harris, H. Hirase, X. Leinekugel, D. A. Henze and G. Buzsáki, Temporal interaction between single spikes and complex spike bursts in hippocampal pyramidal cells, *Neuron* **32**(1) (2001) 141–149.

49. M. C. Quirk, K. I. Blum and M. A. Wilson, Experience-dependent changes in extracellular spike amplitude may reflect regulation of dendritic action potential back-propagation in rat hippocampal pyramidal cells, *J. Neurosci.* **21**(1) (2001) 240–248.

50. C. Pouzat, M. Delescluse, P. Viot and J. Diebolt, Improved spike-sorting by modeling firing statistics and burst-dependent spike amplitude attenuation: A Markov chain monte carlo approach, *J. Neurophysiol.* **91**(6) (2004) 2910–2928.

51. T. Kreuz, J. S. Haas, A. Morelli, H. D. I. Abarbanel and A. Politi, Measuring spike train synchrony, *J. Neurosci. Methods* **165**(1) (2007) 151–161.

52. M. C. W. van Rossum, A novel spike distance, *Neural Comput.* **13**(4) (2001) 751–763.

53. S. Schreiber, J. M. Fellous, J. H. Whitmer, P. H. E. Tiesinga and T. J. Sejnowski, A new correlation-based measure of spike timing reliability, *Neurocomputing* **52–54** (2003) 925–931.

54. J. D. Hunter, G. Milton, P. J. Thomas and J. D. Cowan, Resonance effect for neural spike time reliability, *J. Neurophysiol.* **80**(3) (1998) 1427–1438.

55. R. H. R. Hahnloser, A. A. Kozhevnikov and M. S. Fee, An ultra-sparse code underlies the generation of neural sequences in a songbird, *Nature* **419** (2002) 65–70.

56. H. Peng, F. Long and C. Ding, Feature selection based on mutual information: Criteria of max-dependency, max-relevance, and min-redundancy, *IEEE Trans. Pattern Anal. Mach. Intell.* **27**(8) (2005) 1226–1238.

57. A. Cichocki and S. Amari, Adaptive Blind Signal and Image Processing: Learning Algorithms and Applications, John Wiley & Sons, Inc. New York, NY, USA (2002).

58. S. Ghosh-Dastidar and H. Adeli, Spiking neural networks, *Int. J. Neural Syst.* **19**(4) (2009) 295–308.

59. J. L. Rossello, V. Canals, A. Morro and J. Verd, Chaos-based mixed signal implementation of spiking neurons, *Int. J. Neural Syst.* **19**(6) (2009) 465–471.

60. T. J. Strain, L. J. McDaid, L. P. Maguire and T. M. McGinnity, An STDP training algorithm for a spiking neural network with dynamic threshold neurons, *Int. J. Neural Syst.* **20**(6) (2010) 463–480.

61. A. Vidybida, Testing of information condensation in a model reverberating spiking neural network, *Int. J. Neural Syst.* **21**(3) (2011) 187–198.

62. N. R. Luque, J. A. Garrido, R. R. Carrillo, S. Tolu, and E. Ros, Adaptive cerebral spiking model embedded in the control loop: Context switching and robustness against noise, *Int. J. Neural Syst.* **21**(5) (2011) 385–401.

63. J. Iglesias and A. E. P. Villa, Emergence of preferred firing sequences in large spiking neural networks during simulated neuronal development, *Int. J. Neural Syst.* **18**(4) (2008) 267–277.